

Article

Parameter Identification of Five-Phase Squirrel Cage Induction Motor Based on Extended Kalman Filter

Xiangyu Luo ¹, Jinghong Zhao ¹, Yiyong Xiong ^{1,*}, Hao Xu ¹, Hansi Chen ¹ and Shuheng Zhang ²

¹ School of Electrical Engineering, Naval University of Engineering, Wuhan 430033, China; luoxiangyu0125@163.com (X.L.); zhaojinghong@163.com (J.Z.); xuhao10141205@163.com (H.X.); chenhansi1111@163.com (H.C.)

² College of Electronic and Information Engineering, Jiangxi University of Engineering, Xinyu 338000, China; zhangshuheng0917@163.com

* Correspondence: xiongyiyong1989@163.com

Abstract: The use of multiphase electric drives in industrial applications has increased in the last few years. These machines' advantages over the three-phase system make them appropriate for harsh working situations. To increase their inherent reliability, some authors have been working in sensorless control schemes, where the absence of an encoder ensures proper system performance. Nevertheless, these sensorless control systems present some problems due to the uncertainties of the parameters. In this regard, using extended Kalman filters overcomes this situation, since Kalman filters consider the system error and measurement error in the estimation process. However, when the three-phase Kalman filters are extended to the five-phase case of study, the complexity of the problem increases substantially. In this work, the authors propose an extended Kalman filter, which discomposes the original state equation, reducing the complexity of the estimation stage. In addition, the system suppresses the third-harmonic injection, which enhances the overall phase-current quality.

Keywords: five-phase induction motor; extended Kalman filter; speed sensorless control; parameter identification



Citation: Luo, X.; Zhao, J.; Xiong, Y.; Xu, H.; Chen, H.; Zhang, S. Parameter Identification of Five-Phase Squirrel Cage Induction Motor Based on Extended Kalman Filter. *Processes* **2022**, *10*, 1440. <https://doi.org/10.3390/pr10081440>

Academic Editors: Ján Pitel', Haoming Liu, Jingrui Zhang and Jian Wang

Received: 21 June 2022

Accepted: 19 July 2022

Published: 23 July 2022

Publisher's Note: MDPI stays neutral with regard to jurisdictional claims in published maps and institutional affiliations.



Copyright: © 2022 by the authors. Licensee MDPI, Basel, Switzerland. This article is an open access article distributed under the terms and conditions of the Creative Commons Attribution (CC BY) license (<https://creativecommons.org/licenses/by/4.0/>).

1. Introduction

Induction motors are widely used in wind power generation, train traction, the automotive industry, ship propulsion, and other fields because of their low maintenance cost, good dynamic response, better speed–torque characteristics, and higher efficiency [1–4]. With the development of power electronics technology, the electrical system has overcome the restriction of power supply phase numbers. The increase in phase number also brings many advantages to the motor drive system. Compared with the traditional three-phase motor, the five-phase motor has lower phase voltage, smaller torque ripple, and higher reliability under the same power [5,6]. Nowadays, the multiphase motor possesses the trend of gradually replacing the traditional three-phase motor.

Speed closed-loop control is indispensable in high-performance vector control of induction motors. Generally, speed sensors, such as photoelectric encoders, are coaxially connected with the motor to observe the speed. In harsh working environments, speed sensors are prone to failure. In order to realize the accurate control of speed without speed sensors, speed sensorless vector control has become an important subject in the field of AC drive. The traditional speed sensorless vector control method for induction motors uses stator current and voltage to estimate rotor flux linkage and slip [7]. In addition, model-based speed sensorless induction motor drive technology, which combines the state equation of the induction motor with the signal injection method, is also considered to be a good method to achieve speed sensorless control [8]. These control methods based on signal injection can realize speed sensorless control, but they have high complexity and poor adaptability to the drive system [9]. Traditional speed sensorless control still has some

problems due to the uncertainty of the parameters during the operation of the motor. In order to overcome these uncertainties, several methods based on model estimation, such as a model reference adaptive system, full-order observer, extended Luenberger observer, sliding mode observer, and the extended Kalman filter, have become the main research focuses [10–13]. Different from the deterministic method used in observer designs in model reference adaptive system technology, the extended Kalman filter takes the system error and measurement error into account in the estimation process. The ability to adjust the Kalman filter according to the noise characteristics of measurement and initial disturbance highlights the advantages of the stochastic method over the deterministic method [14,15].

Different from the three-phase induction motor, the vector control of the five-phase induction motor with centralized winding should consider both the fundamental space and the third-harmonic space, and it generally adopts the control method of third-harmonic current suppression [16]. Therefore, when designing an EKF observer, the order of the state equation of the five-phase induction motor is higher than that of the three-phase induction motor. Considering the difference in the state equation of the five-phase induction motor, if the fundamental space and the third-harmonic state-space variables of the five-phase induction motor are controlled at the same time, the state equation of the system will reach the ninth order [17]. If other state variables are introduced, it will be higher and increase the complexity of the system. Therefore, a double EKF structure is proposed in this paper, which can decompose the original ninth-order state equation into a fourth-order and a fifth-order state equation when the third-harmonic current is small. The EKF observer based on this structure can simultaneously observe the rotor angular velocity, fundamental space rotor flux linkage, and third-harmonic space rotor flux linkage.

The rest of this paper is structured as follows: in Section 2, the linear and discrete state equations of the fundamental spatial components of the five-phase squirrel cage induction motor are derived; Section 3 introduces the EKF algorithm and the double EKF structure; then, the results of speed prediction and flux linkage prediction are discussed in Section 4; finally, Section 5 summarizes the research of this paper.

2. Linear, Discrete State-Space Model for Five-Phase Squirrel Cage Induction Motors

Similarly to the three-phase induction motor, the five-phase induction motor can also transform the five-phase voltage and current into the two-phase stationary coordinate system and the two-phase synchronous rotating coordinate system through coordinate transformation. The Clark conversion formula from the five-phase rotating coordinate system to the two-phase stationary coordinate system can be written as [18]:

$$\begin{bmatrix} x_{\alpha 1} \\ x_{\beta 1} \\ x_{\alpha 3} \\ x_{\beta 3} \\ x_0 \end{bmatrix} = \sqrt{\frac{2}{5}} \begin{bmatrix} 1 & \cos\left(\frac{2\pi}{5}\right) & \cos\left(\frac{4\pi}{5}\right) & \cos\left(\frac{6\pi}{5}\right) & \cos\left(\frac{8\pi}{5}\right) \\ 0 & \sin\left(\frac{2\pi}{5}\right) & \sin\left(\frac{4\pi}{5}\right) & \sin\left(\frac{6\pi}{5}\right) & \sin\left(\frac{8\pi}{5}\right) \\ 1 & \cos\left(\frac{4\pi}{5}\right) & \cos\left(\frac{8\pi}{5}\right) & \cos\left(\frac{2\pi}{5}\right) & \cos\left(\frac{6\pi}{5}\right) \\ 0 & \sin\left(\frac{4\pi}{5}\right) & \sin\left(\frac{8\pi}{5}\right) & \sin\left(\frac{2\pi}{5}\right) & \sin\left(\frac{6\pi}{5}\right) \\ \sqrt{\frac{1}{2}} & \sqrt{\frac{1}{2}} & \sqrt{\frac{1}{2}} & \sqrt{\frac{1}{2}} & \sqrt{\frac{1}{2}} \end{bmatrix} \begin{bmatrix} x_a \\ x_b \\ x_c \\ x_d \\ x_e \end{bmatrix} \quad (1)$$

The Park conversion equation from a two-phase stationary coordinate system to a two-phase simultaneous rotational coordinate system can be written as [19]:

$$\begin{bmatrix} x_d \\ x_q \end{bmatrix} = \begin{bmatrix} \cos \theta & \sin \theta \\ -\sin \theta & \cos \theta \end{bmatrix} \begin{bmatrix} x_\alpha \\ x_\beta \end{bmatrix}, \quad x = u, i, \psi \quad (2)$$

where x is voltage, current, or flux linkage. The fundamental space-stator current and rotor flux linkage in the two-phase stationary coordinate system are selected as state variables, and the corresponding state equations are as follows [20]:

$$\begin{aligned}
 \frac{di_{s\alpha 1}}{dt} &= \frac{L_r^2 R_s + L_m^2 R_r}{L_r(L_m^2 - L_s L_r)} i_{s\alpha 1} - \frac{L_m R_r}{L_r(L_m^2 - L_s L_r)} \psi_{r\alpha 1} - \frac{L_m \omega_r}{(L_m^2 - L_s L_r)} \psi_{r\beta 1} - \frac{L_r}{(L_m^2 - L_s L_r)} u_{s\alpha 1} \\
 \frac{di_{s\beta 1}}{dt} &= \frac{L_r^2 R_s + L_m^2 R_r}{L_r(L_m^2 - L_s L_r)} i_{s\beta 1} + \frac{L_m \omega_r}{L_r(L_m^2 - L_s L_r)} \psi_{r\alpha 1} - \frac{L_m R_r}{(L_m^2 - L_s L_r)} \psi_{r\beta 1} - \frac{L_r}{(L_m^2 - L_s L_r)} u_{s\beta 1} \\
 \frac{d\psi_{r\alpha 1}}{dt} &= \frac{L_m R_r}{L_r} i_{s\alpha 1} - \frac{R_r}{L_r} \psi_{r\alpha 1} - \omega_r \psi_{r\beta 1} \\
 \frac{d\psi_{r\beta 1}}{dt} &= \frac{L_m R_r}{L_r} i_{s\beta 1} + \omega_r \psi_{r\alpha 1} - \frac{R_r}{L_r} \psi_{r\beta 1}
 \end{aligned} \tag{3}$$

where L_m , L_s , and L_r are the equivalent mutual inductance, stator-side equivalent self-inductance, and rotor-side equivalent self-inductance, respectively, whose values are 2.5 times the mutual inductance, stator-side self-inductance, and rotor-side self-inductance in the fundamental space of the five-phase squirrel cage induction motor.

The dynamic state-space model of the fundamental space of the five-phase induction motor has four state variables. In order to realize vector control without a speed sensor, the rotor angular velocity is added as a state variable so that the expanded-order system equations of the five-phase induction motor are obtained. Since the Kalman filter algorithm is applicable to linear systems, the digitalization of the algorithm requires the discretization of the algorithm, while the state-space equations of the five-phase squirrel cage induction motor are nonlinear and continuous. Therefore, the state-space equations of the five-phase motor should be linearized and discretized. Consider the linear system shown in Figure 1, whose state and measurement equations can be written as:

$$\begin{aligned}
 \frac{dx(t)}{dt} &= f[x(t)] + Bu(t) + w(t) \\
 y(t) &= h[x(t)] + v(t)
 \end{aligned} \tag{4}$$

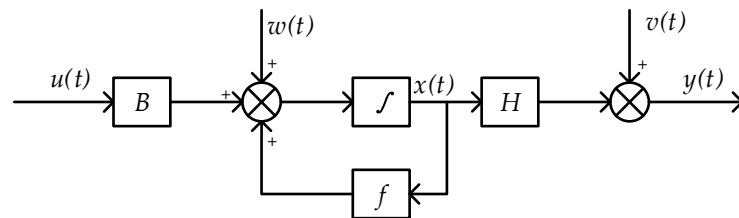


Figure 1. Linear system block diagram.

The Taylor expansion of Equation (4) at $\hat{x}(t)$, retaining the constant and primary terms and rounding off the higher terms, yields:

$$\begin{aligned}
 \frac{dx(t)}{dt} &= f[\hat{x}(t)] + \left. \frac{\partial f[x(t)]}{\partial x(t)} \right|_{x(t)=\hat{x}(t)} \Delta x + Bu(t) + w(t) \\
 y(t) &= h[\hat{x}(t)] + \left. \frac{\partial h[x(t)]}{\partial x(t)} \right|_{x(t)=\hat{x}(t)} \Delta x + v(t)
 \end{aligned} \tag{5}$$

where $\Delta x = x(t) - \hat{x}(t)$. $w(t)$ and $v(t)$ represent system noise and measurement noise, respectively, which are Gaussian white noise with the average expectation of 0.

The linearized state equation is discretized, and assuming that the sampling period T_s is sufficiently small, the following approximation can be made at the moment k :

$$\frac{dx_k}{dt} \approx \frac{x_k - x_{k-1}}{T_s} \tag{6}$$

From Equation (4) to (6), the state equations of the discretized five-phase induction motor base-wave space linear system can be obtained as:

$$\begin{cases} x_k = x_{k-1} + [A_k x_{k-1} + Bu]T_s + w_{k-1} \\ y_k = Hx_k + v_k \end{cases} \tag{7}$$

where:

$$A = \begin{bmatrix} -\frac{R'}{\sigma} & 0 & \frac{L'}{T_r} & L'\omega_r & L'\psi_{r\beta 1} \\ 0 & -\frac{R'}{\sigma} & -L'\omega_r & \frac{L'}{T_r} & -L'\psi_{r\alpha 1} \\ \frac{L_m}{T_r} & 0 & -\frac{1}{T_r} & -\omega_r & -\psi_{r\beta 1} \\ 0 & \frac{L_m}{T_r} & \omega_r & -\frac{1}{T_r} & \psi_{r\alpha 1} \\ 0 & 0 & 0 & 0 & 0 \end{bmatrix}; B = \begin{bmatrix} \frac{1}{\sigma L_s} & 0 \\ 0 & \frac{1}{\sigma L_s} \\ 0 & 0 \\ 0 & 0 \\ 0 & 0 \end{bmatrix};$$

$$H = \begin{bmatrix} 1 & 0 & 0 & 0 & 0 \\ 0 & 1 & 0 & 0 & 0 \end{bmatrix};$$

$$x = [i_{s\alpha 1} \quad i_{s\beta 1} \quad \psi_{r\alpha 1} \quad \psi_{r\beta 1} \quad \omega_r]^T; y = [i_{s\alpha 1} \quad i_{s\beta 1}]^T; u = [u_{s\alpha 1} \quad u_{s\beta 1}]^T$$

$R' = \frac{L_r^2 R_s + L_m^2 R_r}{L_s L_r^2}$; $L' = \frac{L_m}{\sigma L_s L_r}$; $\sigma = 1 - \frac{L_m^2}{L_s L_r}$ is the magnetic flux leakage coefficient and $T_r = \frac{L_r}{R_r}$ is the rotor time constant. Define the system noise matrix $w(k)$ as a 5×1 order matrix, and the covariance matrix $Q = cov(w) = E\{w, w^T\}$ as a 5×5 order matrix. The measurement noise $v(k)$ is a matrix of order 2×1 , and its covariance matrix $R = cov(v) = E\{v, v^T\}$ is a matrix of order 2×2 .

3. Extended Kalman Filtering Algorithm

The application of the extended Kalman filter in the state estimation of the five-phase induction motor is shown in Figure 2. The red dotted box is the prediction part of the extended Kalman filter algorithm, and the blue dotted box is derived from the state-space equation of the motor. The function of the prediction part is to cause the error between the estimated value and the real value to be close to zero through a large number of calculations, so as to achieve the purpose of real-time tracking.

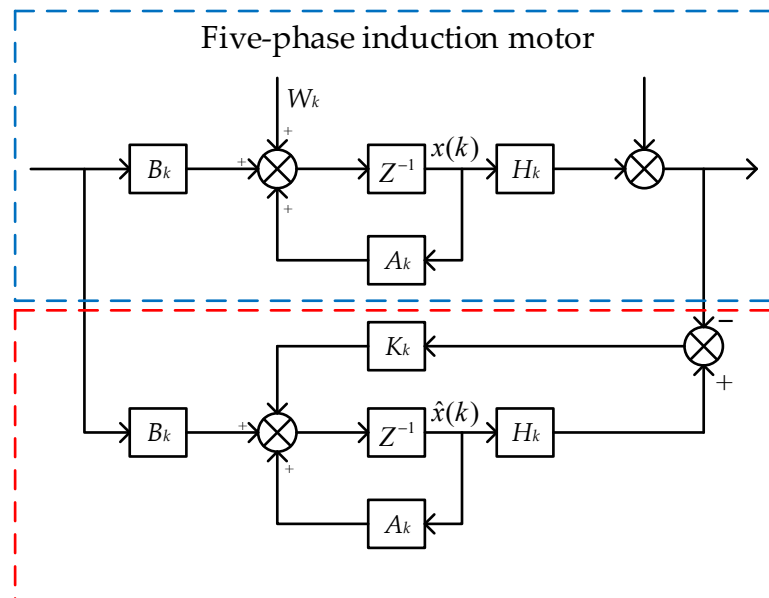


Figure 2. EKF observer.

Assuming that the state estimate \hat{x}_{k-1} at the moment $k - 1$ is a known quantity, the calculation steps of the extended Kalman filter can be written as follows:

A priori prediction step: the state estimate at moment k is predicted based on the state estimate at moment $k - 1$, which is called a priori estimation and has the following expression:

$$\begin{cases} \hat{x}_{k|k-1} = \hat{x}_{k-1|k-1} + (A_{k|k-1} + B_k u_k) T_s \\ \hat{y}_{k|k-1} = H_k \hat{x}_{k|k-1} \end{cases} \quad (8)$$

Calculate the predicted covariance matrix:

$$P_{k|k-1} = F_{k|k-1} P_{k-1|k-1} F_{k|k-1}^T + Q \quad (9)$$

where:

$$F = I + T_s A = \begin{bmatrix} 1 - \frac{T_s R'}{\sigma} & 0 & \frac{T_s L'_s}{T_r} & T_s L' \omega_r & T_s L' \psi_{r\beta 1} \\ 0 & 1 - \frac{T_s R'}{\sigma} & -T_s L' \omega_r & \frac{T_s L'}{T_r} & -T_s L' \psi_{r\alpha 1} \\ \frac{T_s L_m}{T_r} & 0 & 1 - \frac{T_s}{T_r} & -T_s \omega_r & -T_s \psi_{r\beta 1} \\ 0 & \frac{T_s L_m}{T_r} & T_s \omega_r & 1 - \frac{T_s}{T_r} & T_s \psi_{r\alpha 1} \\ 0 & 0 & 0 & 0 & 1 \end{bmatrix};$$

Calculate the Kalman gain $K_{k|k-1}$:

$$K_{k|k-1} = P_{k|k-1} H^T (H P_{k|k-1} H^T + R)^{-1} \quad (10)$$

A posteriori correction step: The optimal solution obtained $\hat{x}_{k|k}$ from the gain $K_{k|k-1}$ calculated by Equation (6) is called the posterior value, and its expression is as follows:

$$\hat{x}_{k|k} = \hat{x}_{k|k-1} + K_{k|k-1} (y_k - \hat{y}_{k|k-1}) \quad (11)$$

Calculate the covariance matrix $P_{k|k}$ for the next moment:

$$P_{k|k} = (I - K_{k|k-1} H) P_{k|k-1} \quad (12)$$

If the fundamental magnetic chain, the third-harmonic magnetic chain, and the rotor angular velocity are to be observed simultaneously, the equation of state of the system as a whole is a matrix of order 9, and a general microcontroller or DSP cannot handle such a huge amount of data. In fact, after suppressing the current in the third-harmonic space, its electromagnetic torque generated in the third-harmonic space can be approximated as 0, and the effect on the rotor angular velocity can be negligible. Based on this, two EKF observers are used to observe the fundamental magnetic chain, the third-harmonic magnetic chain, and the rotor angular velocity. The first EKF observer is used to observe the fundamental magnetic chain and rotor angular velocity, and the second EKF observer is used to observe the third-harmonic magnetic chain. The predicted rotor angular velocity of the first EKF observer is used as the input to the second EKF observer, which is structured as follows.

As shown in Figure 3, EKF1 observes the rotor magnetic chain in the fundamental space and the rotor angular velocity, and EKF2 observes the rotor magnetic chain in the third-harmonic space. The equation of state in the third-harmonic space can be written as:

$$\begin{aligned} \frac{di_{s\alpha 3}}{dt} &= \frac{L_r^2 R_s + L_{m3}^2 R_{r3}}{L_{r3}(L_{m3}^2 - L_{s3} L_{r3})} i_{s\alpha} - \frac{L_{m3} R_{r3}}{L_{r3}(L_{m3}^2 - L_{s3} L_{r3})} \psi_{r\alpha} - \frac{3L_{m3} \omega_r}{(L_{m3}^2 - L_{s3} L_{r3})} \psi_{r\beta} - \frac{L_{r3}}{(L_{m3}^2 - L_{s3} L_{r3})} u_{s\alpha 3} \\ \frac{di_{s\beta 3}}{dt} &= \frac{L_r^2 R_s + L_{m3}^2 R_{r3}}{L_{r3}(L_{m3}^2 - L_{s3} L_{r3})} i_{s\beta 3} + \frac{3L_{m3} \omega_r}{L_{r3}(L_{m3}^2 - L_{s3} L_{r3})} \psi_{r\alpha 3} - \frac{L_{m3} R_{r3}}{(L_{m3}^2 - L_{s3} L_{r3})} \psi_{r\beta} - \frac{L_{r3}}{(L_{m3}^2 - L_{s3} L_{r3})} u_{s\beta 3} \\ \frac{d\psi_{r\alpha 3}}{dt} &= \frac{L_{m3} R_{r3}}{L_{r3}} i_{s\alpha 3} - \frac{R_{r3}}{L_{r3}} \psi_{r\alpha 3} - 3\omega_r \psi_{r\beta 3} \\ \frac{d\psi_{r\beta 3}}{dt} &= \frac{L_{m3} R_{r3}}{L_{r3}} i_{s\beta 3} + 3\omega_r \psi_{r\alpha 3} - \frac{R_{r3}}{L_{r3}} \psi_{r\beta 3} \end{aligned} \quad (13)$$

where $\hat{\psi}_{r\alpha 1}$ and $\hat{\psi}_{r\beta 1}$ are the predicted flux linkage in the fundamental space in the two-phase stationary coordinate system. $\hat{\omega}_r$ is the predicted angular velocity. $\hat{\psi}_{r\alpha 3}$ and $\hat{\psi}_{r\beta 3}$ are the predicted flux linkage of the third-harmonic space in the two-phase stationary coordinate system.

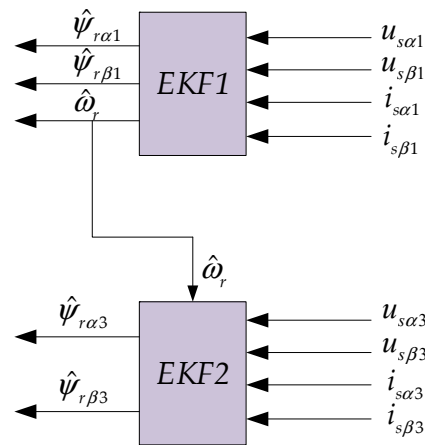


Figure 3. Double EKF observer.

Similarly, the equation of state in the third-harmonic space after linearizing and discretizing Equation (13) can be written as:

$$\begin{cases} \mathbf{x}'_k = \mathbf{x}'_{k-1} + [\mathbf{A}'_k \mathbf{x}'_{k-1} + \mathbf{B}' \mathbf{u}'] T_s + \mathbf{w}'_{k-1} \\ \mathbf{y}'_k = \mathbf{H}' \mathbf{x}'_k + \mathbf{v}'_k \end{cases} \quad (14)$$

where:

$$\mathbf{A}' = \begin{bmatrix} -\frac{R'_3}{\sigma_3} & 0 & \frac{3L'_3}{T_{r3}} & L_3 \omega_r \\ 0 & -\frac{R'_3}{\sigma_3} & -L_3 \omega_r & \frac{3L'_3}{T_{r3}} \\ \frac{L_{m3}}{T_{r3}} & 0 & -\frac{1}{T_{r3}} & -3\omega_r \\ 0 & \frac{L_{m3}}{T_{r3}} & 3\omega_r & -\frac{1}{T_{r3}} \end{bmatrix}; \mathbf{B}' = \begin{bmatrix} \frac{1}{\sigma_3 L_{s3}} & 0 \\ 0 & \frac{1}{\sigma_3 L_{s3}} \\ 0 & 0 \\ 0 & 0 \end{bmatrix}; \mathbf{H}' = \begin{bmatrix} 1 & 0 & 0 & 0 \\ 0 & 1 & 0 & 0 \end{bmatrix};$$

$$\mathbf{x}' = [i_{s\alpha3} \quad i_{s\beta3} \quad \psi_{r\alpha3} \quad \psi_{r\beta3}]^T; \mathbf{y}' = [i_{s\alpha3} \quad i_{s\beta3}]^T; \mathbf{u}' = [u_{s\alpha3} \quad u_{s\beta3}]^T;$$

$R'_3 = \frac{L_{r3}^2 R_s + L_{m3}^2 R_{r3}}{L_{s3} L_{r3}^2}$; $L_3 = \frac{L_{m3}}{\sigma_3 L_{s3} L_{r3}}$; $\sigma_3 = 1 - \frac{L_{m3}^2}{L_{s3} L_{r3}}$ is the magnetic flux leakage coefficient of the third-harmonic space, and $T_{r3} = \frac{L_{r3}}{R_{r3}}$ is the torque constant of the third-harmonic space. Define the system noise matrix $\mathbf{w}(k)$ as a 4×4 order matrix and the covariance matrix $\mathbf{Q}' = \text{cov}(\mathbf{w}') = E\{\mathbf{w}', \mathbf{w}'^T\}$ as a 4×4 order matrix. The measurement noise $\mathbf{v}(k)$ is a matrix of order 2×1 and its covariance matrix $\mathbf{R}' = \text{cov}(\mathbf{v}') = E\{\mathbf{v}', \mathbf{v}'^T\}$ is a matrix of order 2×2 .

The initial parameter settings of the EKF observer are critical, especially the initial values of the system noise matrix \mathbf{Q} , the measurement noise covariance matrix \mathbf{R} , and the prediction covariance matrix \mathbf{P} . The selection of these initial parameters directly determines the overall performance of the algorithm, and the improper selection of initial values can lead to scattering of the whole system.

For the system noise covariance matrix \mathbf{Q} , it mainly includes the system external disturbances, motor parameter variation effects, and errors in the linearization discretization process. If \mathbf{Q} becomes larger, it means that the system noise becomes stronger, indicating that the weighting effect of the measurement feedback is enhanced, and the EKF transient response becomes faster [21].

For the measurement noise covariance matrix \mathbf{R} , it mainly includes the actual sensor measurement error, microcontroller sampling error, and other factors. If \mathbf{R} is increased, it corresponds to a larger deviation in the current measurement, weakening the weight of the algorithm's predicted value, which will lead to a slower transient response [21].

For the error covariance matrix \mathbf{P} , its initial state is generally chosen to be a diagonal array with all elements equal, which has a large effect on the convergence rate of the EKF and the amplitude of the transient state, with little effect on the steady state [22].

The selection of these matrices is related to the parameters of the motor body and is generally obtained using a trial-and-error approach. After a large number of trial-and-error values, the initial values were taken as follows:

$$\begin{aligned}
 Q &= \text{diag}[0.5, 0.5, 5 \times 10^{-5}, 5 \times 10^{-5}, 5 \times 10^{-3}] \\
 R &= \text{diag}[0.05, 0.05] \\
 P &= \text{diag}[1, 1, 1, 1, 1] \\
 Q' &= \text{diag}[0.5, 0.5, 5 \times 10^{-5}, 5 \times 10^{-5}] \\
 R' &= \text{diag}[0.05, 0.05] \\
 P' &= \text{diag}[1, 1, 1, 1]
 \end{aligned}$$

In the EKF speed sensorless control system, SVPWM modulation is used [23]. The control strategy is IRFOC (indirect field-oriented control) [24,25]. The five-phase inverter is an H-bridge structure, and the overall flow chart is shown in Figure 4.

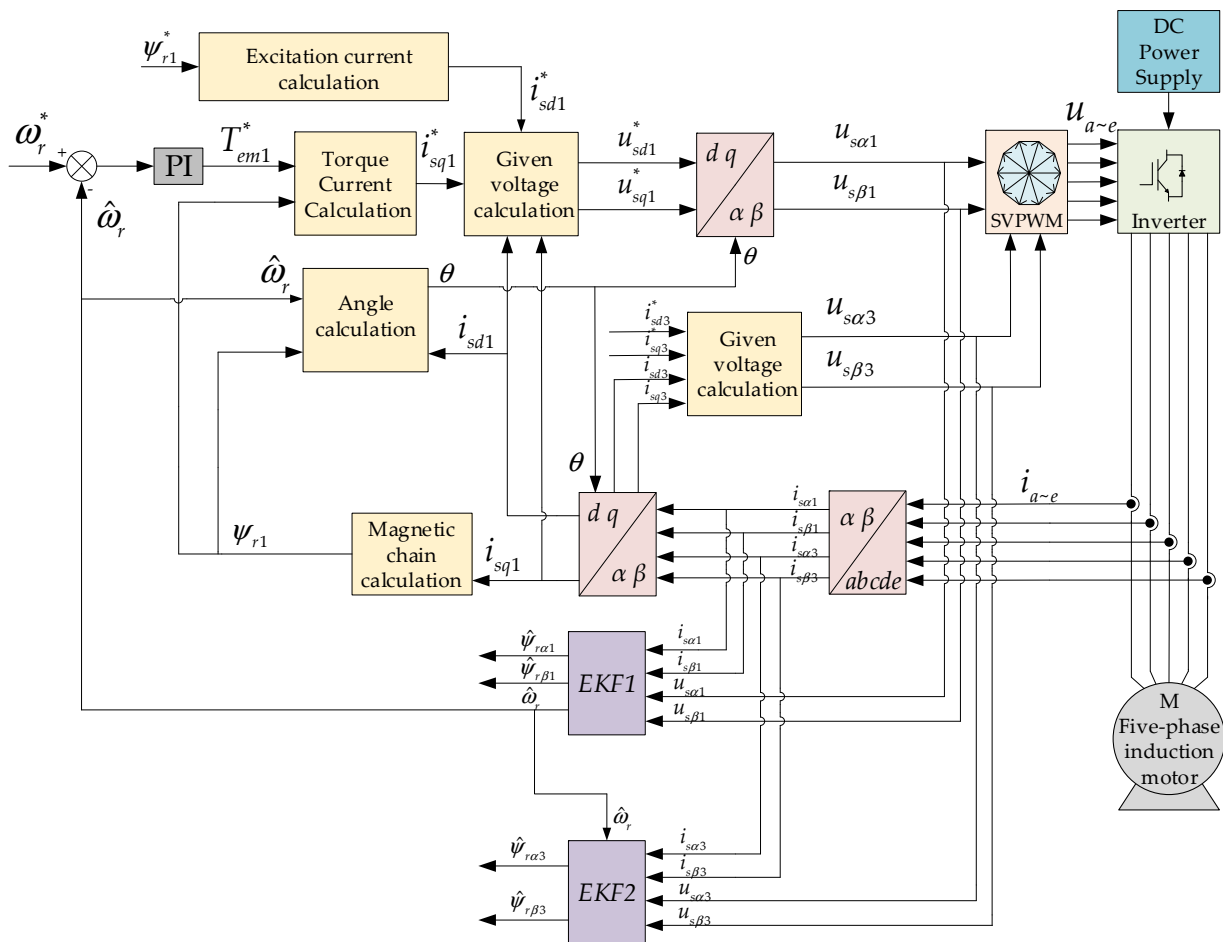


Figure 4. EKF speed sensorless control flow chart.

The current voltage conversion module includes two PI controllers, which use the difference between the measured current and the reference current. The PI controller estimates the voltage necessary to minimize this current difference. For the fundamental space, the current given signals i_{sd1}^* and i_{sq1}^* are calculated from the given torque signal T_{em1}^* and the given flux signal ψ_{r1}^* , respectively. The given torque signal is derived from the predicted speed and the error signal of the given speed through a PI controller. For the third-harmonic space, the given current signals i_{sd3}^* and i_{sq3}^* are set to 0 to achieve the effect of restraining the third-harmonic current.

4. Results and Discussion

In order to verify the effectiveness of the EKF algorithm in the control of a five-phase motor without a speed sensor, a simulation model of it was built in Matlab/Simulink in this study, and the EKF speed sensorless vector control system shown in Figure 4 was established. Among them, the motor parameters used were as seen in Table 1, and its modeling in Simulink is shown in Figure 5.

Table 1. Motor parameters.

Parameter	Symbol	Value
Stator resistance	R_s	0.95 Ω
Fundamental space rotor resistance	R_{r1}	0.78 Ω
Third-harmonic space rotor resistance	R_{r3}	0.52 Ω
Fundamental space spatial mutual inductance	L_{m1}	99.35 mH
Third-harmonic space mutual inductance	L_{m3}	11.04 mH
Fundamental space-stator leakage inductance	L_{sloss1}	6.87 mH
Fundamental space rotor leakage inductance	L_{rloss1}	4.04 mH
Third-harmonic space stator leakage inductance	L_{sloss3}	3.86 mH
Third-harmonic space rotor leakage inductance	L_{rloss3}	3.76 mH
Magnetic pole pairs	n_p	2
Rotational inertia	J	0.056 kg·m ²
Rated speed	n_N	1410 rpm
Rated voltage	U_N	380 V
Rated frequency	f_N	50 Hz
Rated field current	I_{sm}	3.86 A

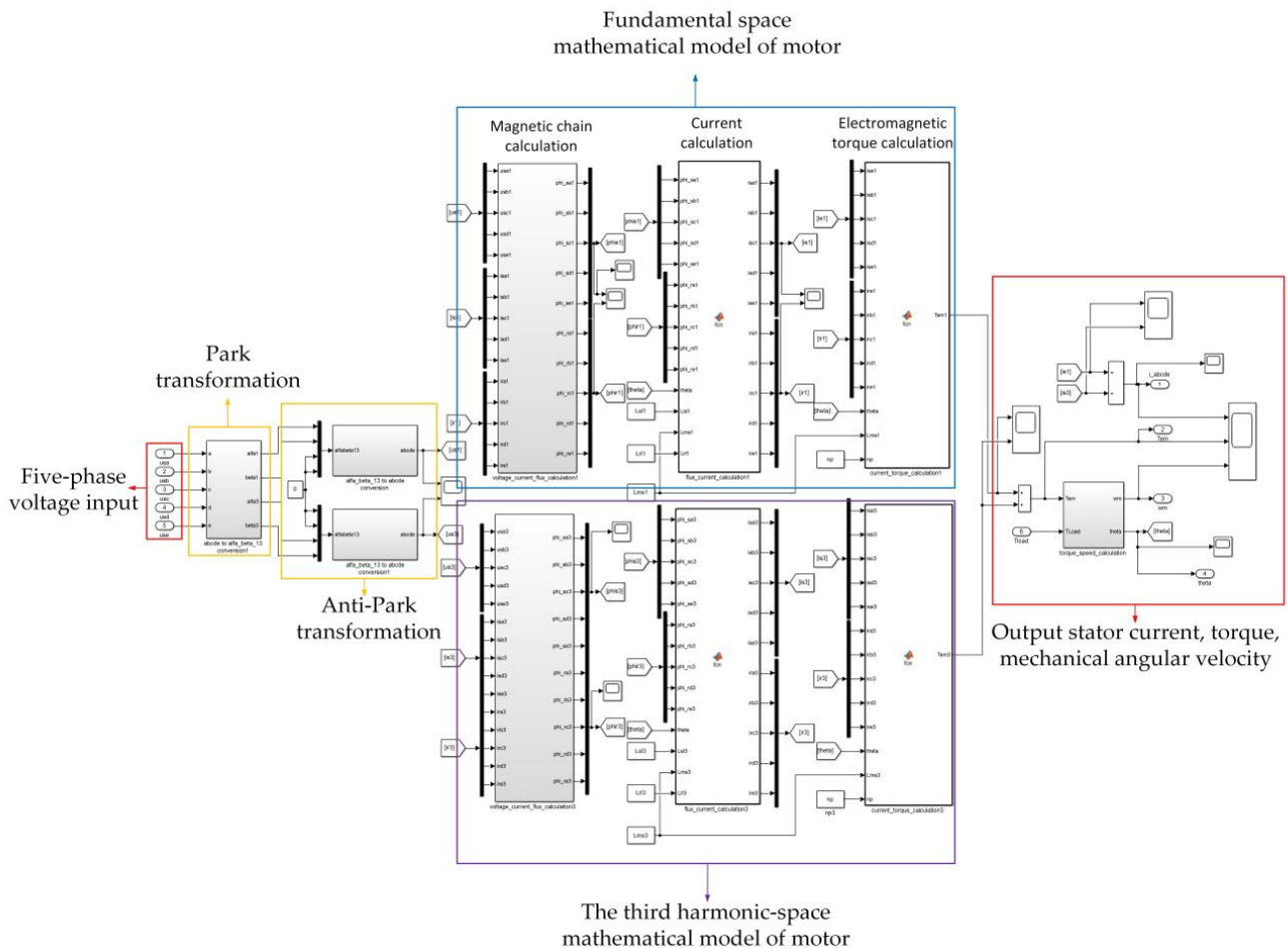


Figure 5. The simulation model of the five-phase induction motor.

The model is mainly divided into five modules: coordinate transformation modules, voltage–magnetic chain modules, magnetic chain–current modules, current–electromagnetic torque modules, and electromagnetic torque–speed modules. The coordinate transformation module is based on the five-phase Clark transformation matrix and its inverse transform matrix. The five-phase voltage is decoupled to the fundamental space and three-harmonic space of the $\alpha\beta$ coordinate system, and then the transformation is converted them into the ABCDE five-phase voltage. In the voltage–magnetic chain module, the magnetic chain is calculated using the input voltage, current, and motor resistance. The magnetic chain–current module uses the inductive matrix and each phase magnetic chain to obtain the current. The torque–speed module mainly calculates motor rotor rotation speed.

4.1. Speed Prediction under Different Working Conditions

In order to verify whether the EKF algorithm can replace the traditional speed sensor, first, the feedback value of the speed loop was changed to the real speed of the motor. Here, EKF was used as an observer. The whole system adopted indirect field-oriented control structure. At that time, the comparison between the predicted speed of the EKF algorithm and the speed of indirect field vector control with a speed sensor is shown in Figure 6.

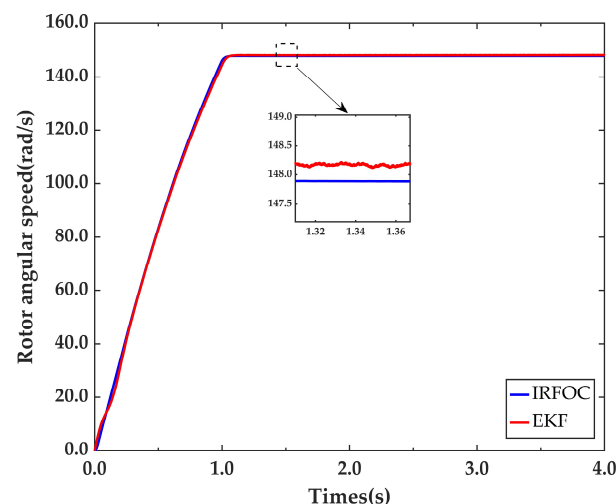


Figure 6. The performance of the EKF observer.

As shown in Figure 6, different from the vector control, the EKF algorithm introduced an error matrix in the iterative operation process, so the pulsation of speed waveform given by the EKF algorithm was larger than the real speed of IRFOC. Under the rated working condition, the EKF algorithm was accurate in observing the change in the rotating speed. Therefore, the EKF algorithm can replace the traditional speed sensor. Based on this premise, the structure of Figure 4 was adopted in the subsequent simulation, and the speed predicted by EKF was directly substituted into the speed closed-loop.

To verify the speed tracking performance of the algorithm, four working conditions shown in Table 2 were selected for simulation:

Table 2. Different working conditions.

Working Condition	Rotor Angular Speed Setting	Load Torque Setting
1	0~4 s:100 rad/s	0~4 s:0 N·m
2	0~4 s:100 rad/s	0~4 s:6 N·m
3	0~1.5 s:60 rad/s/1.5~3 s:90 rad/s/3~4 s:30 rad/s	0~4 s:0 N·m
4	0~1.5 s:100 rad/s/1.5~4 s:−100 rad/s	0~4 s:0 N·m

The four working conditions in Table 2 were used to test the speed prediction performance of the EKF algorithm under no-load, on load, acceleration and deceleration, and forward and reverse rotation. It can be seen from Figure 7 that the EKF algorithm had a good speed prediction performance under these four working conditions. It can be seen from Figure 7a that, when the speed reached the given speed, there was a steady-state error of about 0.5 rad/s between the EKF algorithm and the actual speed. It can be seen from Figure 7b–d that, when the given speed changed suddenly or the load was added, a small error occurred between the predicted speed and the real speed, and then the predicted speed quickly converged to the actual speed. This showed that the overall robustness of the system was good, and it can be applied to the conditions requiring a wide range of speed regulation.

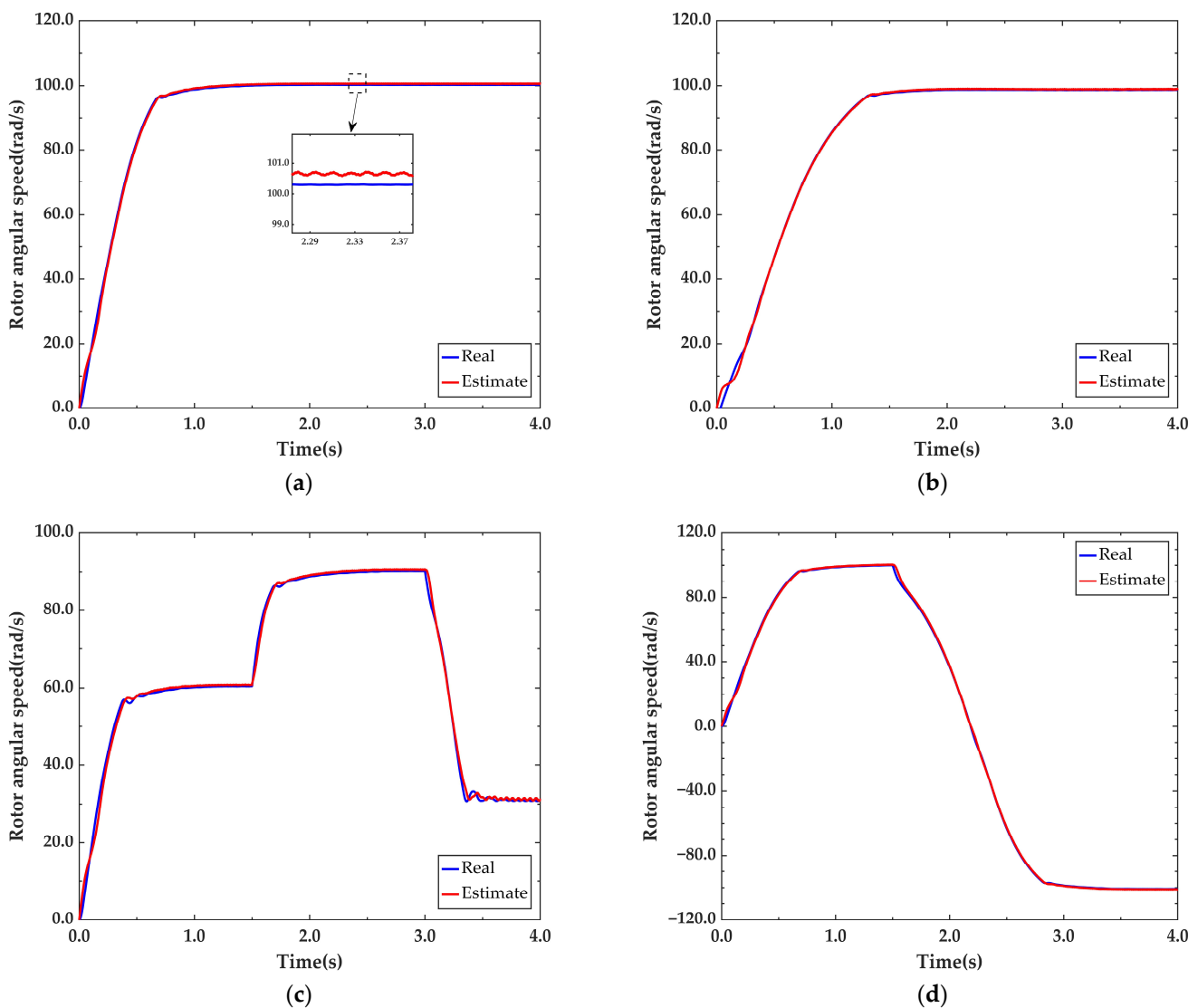


Figure 7. Speed prediction under different working conditions. (a) Condition 1; (b) Condition 2; (c) Condition 3; (d) Condition 4.

4.2. Rotor Flux Identifications

The rated field current of the motor used in this simulation was 3.86 A, so the rated fundamental space given flux linkage can be calculated as 0.96 Wb from Equation (15). In order to verify the flux linkage prediction ability of the EKF algorithm, the simulation was

conducted by changing the field current to 50%, 64%, 84%, and 100% of the rated field current under condition 1 in Table 2.

$$\psi_{ref} = 2.5I_{sm}L_{m1} \quad (15)$$

Similarly, according to formula (15), when the field current was 50%, 64%, and 84% of the rated value, the corresponding fundamental space given flux linkage was 0.48 Wb, 0.61 Wb, and 0.81 Wb. For the third-harmonic spatial flux linkage, its given value is always 0, so its predicted flux linkage was also about 0.

It can be seen from Figure 8 that the EKF algorithm could accurately predict the change in rotor flux linkage in the fundamental space in a steady state. Table 3 lists the predicted values and error values in four cases. It can be seen that the prediction error of flux linkage accounted for about 10% of the given value. In addition, the estimated value of the flux linkage fluctuated slightly in the steady state. This is because the rotor position angle in the IRFOC method estimated the position of the magnetic flux relative to the stator by integrating the slip frequency and the actual rotor angular speed. In the simulation experiment, the predicted rotor angular velocity was used instead of the actual rotor angular velocity. However, there was a small error between the predicted speed and the actual speed. Therefore, the calculated rotor position angular velocity also deviated from the reality, resulting in a small pulsation of the flux linkage in the steady state.

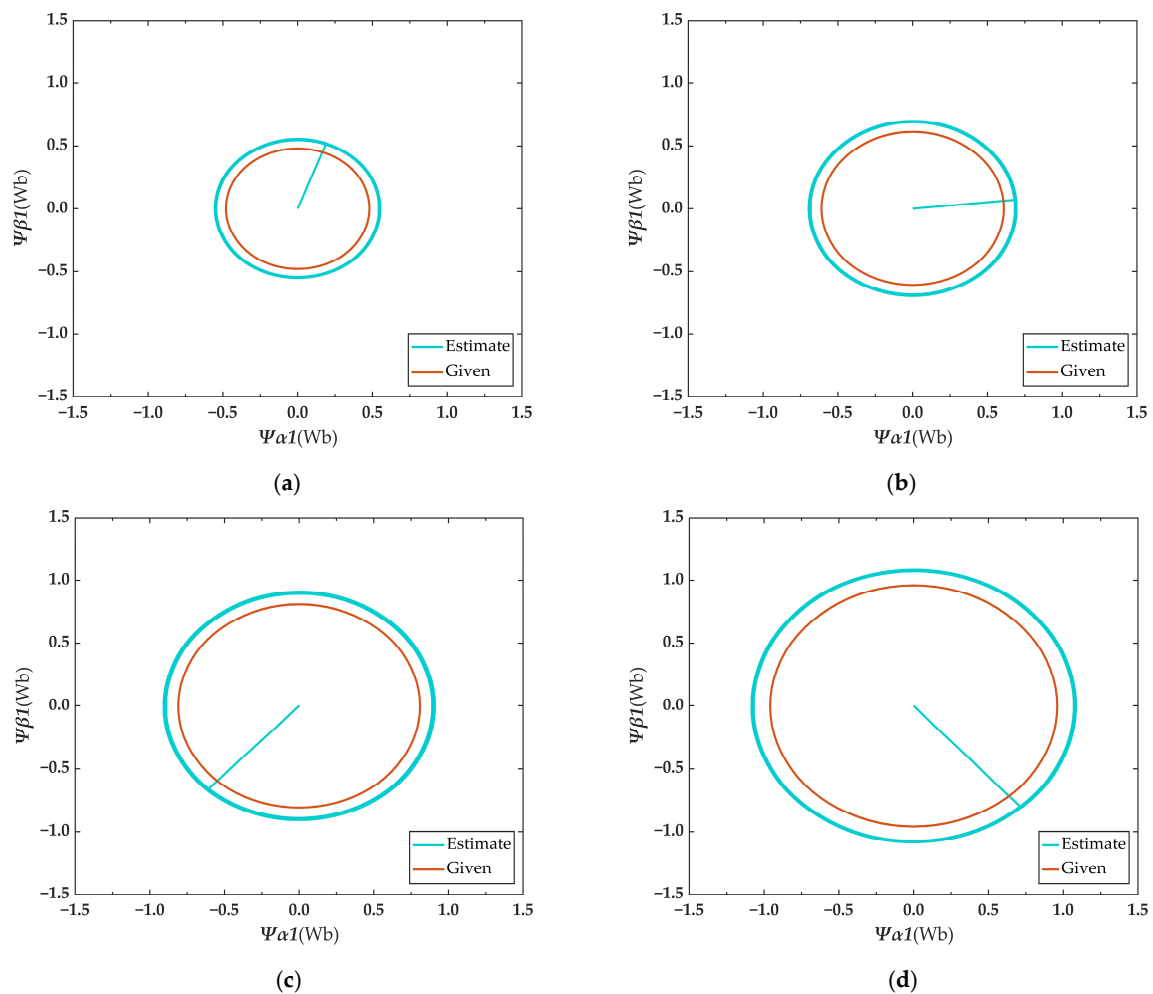


Figure 8. The prediction of fundamental space rotor flux linkage. (a) 50% of rated field current; (b) 64% of rated field current; (c) 84% of rated field current; (d) rated field current.

Table 3. Prediction error of fundamental space rotor flux linkage.

Working Condition (Flux Linkage Amplitude)	Predicted Flux Linkage Value	Error Value
50% of rated field current (0.48 Wb)	0.54 Wb	0.06 Wb
64% of rated field current (0.61 Wb)	0.68 Wb	0.07 Wb
84% of rated field current (0.81 Wb)	0.89 Wb	0.08 Wb
Rated field current (0.96 Wb)	1.06 Wb	0.10 Wb

It can be seen from Figure 9 that the predicted flux linkage of the third-harmonic in four cases was about 0, which also indicated that the third-harmonic current was effectively suppressed when the field current was changed.

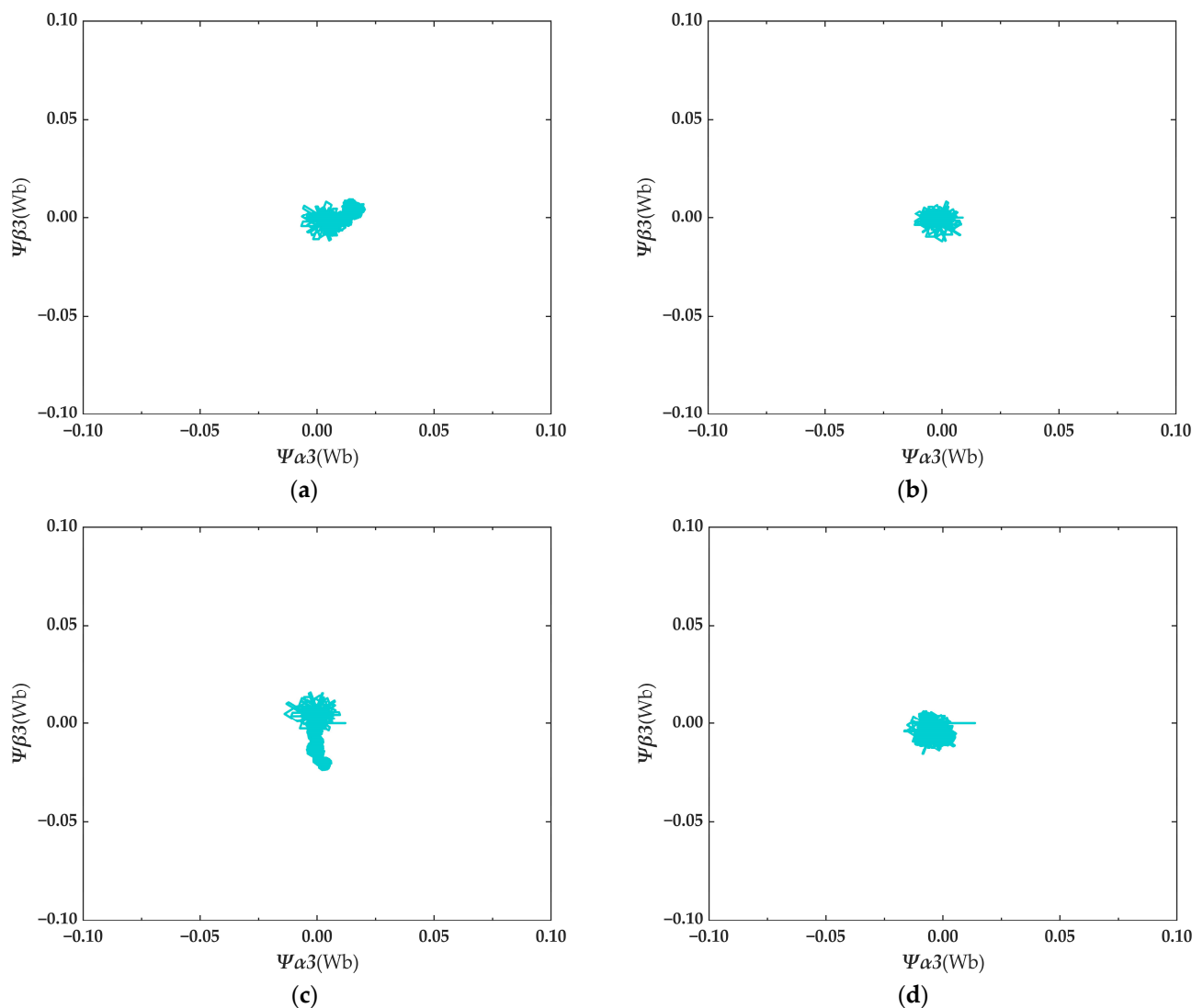


Figure 9. The prediction of third-harmonic space rotor flux linkage. (a) 50% of rated field current; (b) 64% of rated field current; (c) 84% of rated field current; (d) rated field current.

4.3. Third-Harmonic Current Suppression Effect

Figures 10 and 11 show the stator current waveform and the stator third-harmonic current waveform under condition 1 in Table 2. It can be seen from Figure 10 that the overall sinusoidal degree of the stator current was good, and its FFT analysis is shown in Figure 12. According to Figure 12, when the given speed was 100 rad/s, the corresponding stator current frequency was 31.83 Hz, and the THD of the stator current was 8.58%, indicating

that the third-harmonic current had been effectively suppressed. It can be seen from Figure 10 that most of the third-harmonic currents were distributed below the amplitude of 0.6 A in the steady state.

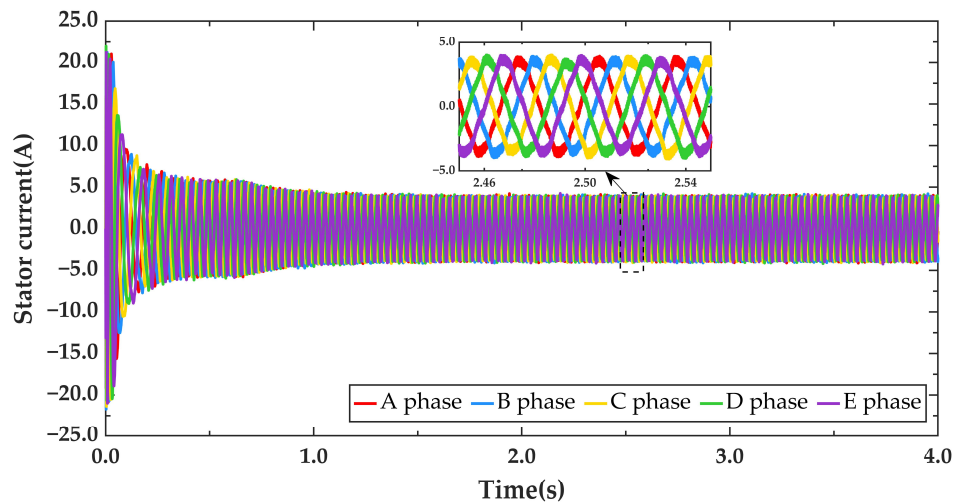


Figure 10. Stator current.

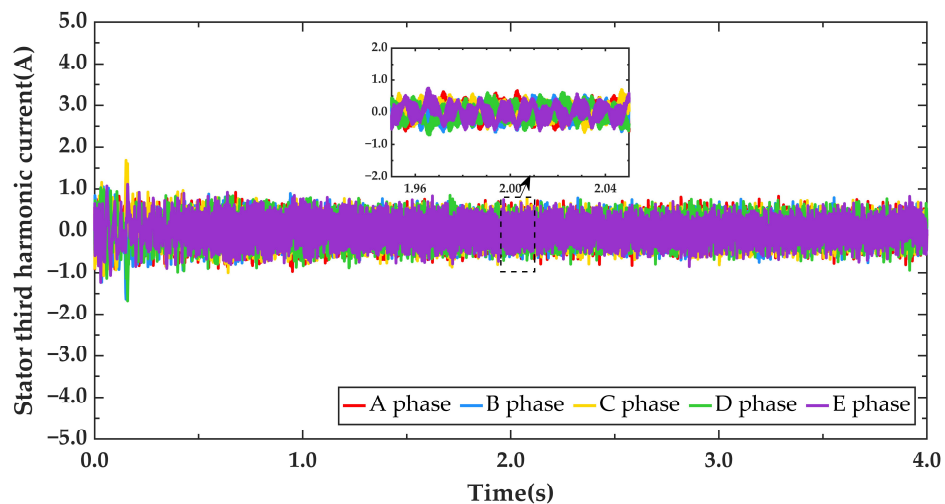


Figure 11. Stator current (third-harmonic space).

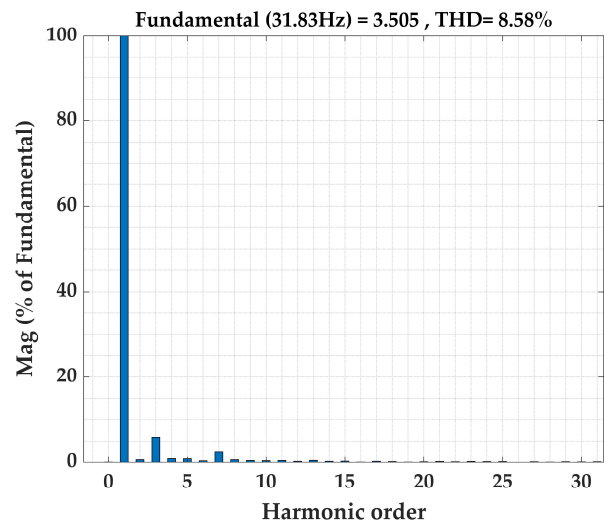


Figure 12. FFT analysis of stator current.

5. Conclusions

In this study, the EKF algorithm was extended to the parameter identification of the five-phase squirrel cage induction motor, and the theoretical part was derived in detail. On the premise of restraining the third-harmonic current of the motor, a new double EKF structure was proposed, which simplified the state equation of the system. The simulation results showed that the EKF algorithm was accurate in predicting the rotor angular speed, and the algorithm was suitable for the sensorless control of the five-phase squirrel cage induction motor, which needs a wide range of speed regulation. The EKF algorithm could observe the rotor flux linkage, but there was an error between the predicted value and the given value, which was about 10% of the given value. In view of the shortcomings of this paper, the follow-up research direction could be to reduce the order of the state equation of the whole system without the third-harmonic current suppression.

Author Contributions: Data curation, X.L. and J.Z.; Methodology, X.L.; Resources, H.C. and S.Z.; Software, H.X.; Writing—original draft, X.L.; Writing—review and editing, Y.X. All authors have read and agreed to the published version of the manuscript.

Funding: This research received no external funding.

Institutional Review Board Statement: Not applicable.

Informed Consent Statement: Not applicable.

Data Availability Statement: Not applicable.

Acknowledgments: Thanks to J.Z. for providing guidance on the data analysis of this article, Y.X., H.X., H.C. and S.Z. for revising and sorting this article.

Conflicts of Interest: The authors declare no conflict of interest.

References

1. Benbouhenni, H.; Bizon, N. A Synergetic Sliding Mode Controller Applied to Direct Field-Oriented Control of Induction Generator-Based Variable Speed Dual-Rotor Wind Turbines. *Energies* **2021**, *14*, 4437. [[CrossRef](#)]
2. De Pancorbo, S.M.; Ugalde, G.; Poza, J.; Egea, A. Comparative Study between Induction Motor and Synchronous Reluctance Motor for Electrical Railway Traction Applications. In Proceedings of the 5th International Electric Drives Production Conference (EDPC), Nuremberg, Germany, 15–16 September 2015.
3. Gnacinski, P.; Tarasiuk, T.; Mindykowski, J.; Peplinski, M.; Gorniak, M.; Hallmann, D.; Pillat, A. Power Quality and Energy-Efficient Operation of Marine Induction Motors. *IEEE Access* **2020**, *8*, 152193–152203. [[CrossRef](#)]
4. Yang, Z.; Shang, F.; Brown, I.P.; Krishnamurthy, M. Comparative Study of Interior Permanent Magnet, Induction, and Switched Reluctance Motor Drives for EV and HEV Applications. *IEEE Trans. Transp. Electrification* **2015**, *1*, 245–254. [[CrossRef](#)]
5. Pandey, R.; Panda, A.K.; Patnaik, N. Comparative Performance Analysis of DTC fed Three-Phase and Five-Phase Induction Motor. In Proceedings of the 5th International Conference on Devices, Circuits and Systems (ICDCS), Coimbatore, India, 5–6 March 2020; pp. 162–166.
6. Sarwer, Z.; Sartaj, M.; Khan, M.R.; Zaid, M.; Shahajhani, U. Comparative Performance Study of Five-Phase Induction Motor. In Proceedings of the IEEE International Conference on Innovations in Power and Advanced Computing Technologies, Vellore, India, 22–23 March 2019.
7. Holtz, J. Sensorless control of induction motor drives. *Proc. IEEE* **2002**, *90*, 1359–1394. [[CrossRef](#)]
8. Piippo, A.; Salomaki, J.; Luomi, J. Signal injection in sensorless PMSM drives equipped with inverter output filter. *IEEE Trans. Ind. Appl.* **2008**, *44*, 1614–1620. [[CrossRef](#)]
9. Shivaramakrishna, K.V.; Chauhan, A.K.; Raghuram, M.; Singh, S.K. Sensorless Control of Induction Motor using EKF: Analysis of Parameter Variation on EKF Performance. In Proceedings of the IEEE International Conference on Power Electronics, Drives, and Energy Systems (PEDES), Trivandrum, India, 14–17 December 2016.
10. Accetta, A.; Cirrincione, M.; Pucci, M.; Vitale, G. Neural Sensorless Control of Linear Induction Motors by a Full-Order Luenberger Observer Considering the End Effects. *IEEE Trans. Ind. Appl.* **2014**, *50*, 1891–1904. [[CrossRef](#)]
11. Comanescu, M. Design and Implementation of a Highly Robust Sensorless Sliding Mode Observer for the Flux Magnitude of the Induction Motor. *IEEE Trans. Energy Convers.* **2016**, *31*, 656–664. [[CrossRef](#)]
12. Korzonek, M.; Tarchala, G.; Orłowska-Kowalska, T. A review on MRAS-type speed estimators for reliable and efficient induction motor drives. *ISA Trans.* **2019**, *93*, 1–13. [[CrossRef](#)] [[PubMed](#)]
13. Salim, R.; Mansouri, A.; Bendiabdellah, A.; Chekroun, S.; Touam, M. Sensorless passivity based control for induction motor via an adaptive observer. *ISA Trans.* **2019**, *84*, 118–127. [[CrossRef](#)] [[PubMed](#)]

14. Barut, M.; Bogosyan, S.; Gokasan, M. Speed-sensorless estimation for induction motors using extended Kalman filters. *IEEE Trans. Ind. Electron.* **2007**, *54*, 272–280. [[CrossRef](#)]
15. Shi, K.L.; Chan, T.F.; Wong, Y.K.; Ho, S.L. Speed estimation of an induction motor drive using an optimized extended Kalman filter. *IEEE Trans. Ind. Electron.* **2002**, *49*, 124–133. [[CrossRef](#)]
16. Feng, Y.X.; Liao, Y.; Zhang, X.K. A Third Harmonic Current Elimination Strategy for Symmetrical Six-Phase Permanent Magnet Synchronous Motor. *IEEE Access* **2021**, *9*, 167570–167579. [[CrossRef](#)]
17. Bounasla, N.; Barkat, S.; Benyoussef, E.; Tounsi, K. Sensorless Sliding Mode Control of a Five-Phase PMSM using Extended Kalman Filter. In Proceedings of the 8th International Conference on Modelling, Identification and Control (ICMIC), Algiers, Algeria, 15–17 November 2016; pp. 97–102.
18. Parsa, L.; Toliyat, H.A. Five-phase permanent-magnet motor drives. *IEEE Trans. Ind. Appl.* **2005**, *41*, 30–37. [[CrossRef](#)]
19. González, O.; Rodas, J.; Gregor, R.; Ayala, M.; Rivera, M. Speed sensorless predictive current control of a five-phase induction machine. In Proceedings of the 2017 12th IEEE Conference on Industrial Electronics and Applications (ICIEA), Siem Reap, Cambodia, 18–20 June 2017; pp. 343–348.
20. Wen-Jieh, W.; Chun-Chieh, W. A rotor-flux-observer-based composite adaptive speed controller for an induction motor. *IEEE Trans. Energy Convers.* **1997**, *12*, 323–329. [[CrossRef](#)]
21. Bolognani, S.; Tubiana, L.; Zigliotto, M. Extended Kalman filter tuning in sensorless PMSM drives. *IEEE Trans. Ind. Appl.* **2003**, *39*, 1741–1747. [[CrossRef](#)]
22. Janiszewski, D. Extended kalman filter based speed sensorless PMSM control with load reconstruction. In Proceedings of the 32nd Annual Conference of the IEEE-Industrial-Electronics-Society, Paris, France, 7–10 November 2006; pp. 4186–4189.
23. Zheng, L.; Fletcher, J.E.; Williams, B.W.; He, X. Dual-Plane Vector Control of a Five-Phase Induction Machine for an Improved Flux Pattern. *IEEE Trans. Ind. Electron.* **2008**, *55*, 1996–2005. [[CrossRef](#)]
24. Abbasi, H.; Ghanbari, M.; Ebrahimi, R.; Jannati, M. IRFOC of Induction Motor Drives Under Open-Phase Fault Using Balanced and Unbalanced Transformation Matrices. *IEEE Trans. Ind. Electron.* **2021**, *68*, 9160–9173. [[CrossRef](#)]
25. Consoli, A.; Scarcella, G.; Testa, A. Slip frequency detection for indirect field oriented control drives. *IEEE Trans. Ind. Appl.* **2004**, *40*, 194–201. [[CrossRef](#)]